



Anode microstructures from high-energy and high-power lithium-ion cylindrical cells obtained by X-ray nano-tomography



Moses Ender*, Jochen Joos, André Weber, Ellen Ivers-Tiffée

Karlsruhe Institute of Technology (KIT), Institut für Werkstoffe der Elektrotechnik (IWE), Adenauerring 20b, 76131 Karlsruhe, Germany

HIGHLIGHTS

- Graphite anodes from power and energy cells are characterized by HR X-ray nano-CT.
- Microstructure quantification by calculating characteristic structural parameters.
- First direct comparison of microstructures from a high-energy and a high-power cell.
- Discussion of differences in the microstructures and the effects on performance.
- Ion transport in the pores limits performance of the energy cell anode.

ARTICLE INFO

Article history:

Received 6 May 2014

Received in revised form

19 June 2014

Accepted 9 July 2014

Available online 22 July 2014

Keywords:
Lithium-ion
Negative electrode
Microstructure
High-energy
High-power
X-ray tomography

ABSTRACT

Graphite negative electrodes from a high-power and a high-energy cylindrical lithium-ion cell are reconstructed using X-ray nano-tomography. Large volumes and high resolution are required for an in-depth comparison of the design aspects for high-power and high-energy anode. Hence, quite big volumes of $2.37 \cdot 10^6 \mu\text{m}^3$ and $1.27 \cdot 10^6 \mu\text{m}^3$ have to be analyzed to cover the entire thickness of both anode layers. High resolutions of 273 nm and 233 nm voxel size are chosen for assessing volume specific graphite surface area, among other parameters, precisely. A hysteresis segmentation method is adapted for segmentation, featuring a symmetrical growing of both graphite and pore phase. Surface areas are calculated using the marching cube algorithm, particle sizes are calculated based on the Euclidean distance transform (EDT) and tortuosity values are calculated by solving the transport equation using a finite volume scheme in MATLAB. Analysis of these parameters leads to the assumption, that the electrolyte transport is limited by the pore structure of the high-energy graphite anode.

© 2014 Elsevier B.V. All rights reserved.

1. Introduction

The lithium-ion cells in today's state-of-the-art applications are optimized for their intended use which can be classified by two basic categories. First, this are applications which require high energy content such as mobile electronic devices (cell phones, tablet pcs and laptops), where a long-lasting battery operation is demanded. Second, this are applications with a high power consumption such as power tools (e.g. cordless screwdriver), requiring a high power for a limited time. Therefore, lithium-ion cells can be categorized in (a) high-power cells and (b) high-energy cells.

The chemistry of the active material is only one possible difference between these two types of lithium-ion cells. Especially for the anodes (negative electrodes), graphitic carbon is used as anode active material in almost all cells. The difference between a graphite anode of a high-power cell and of a high-energy cell must therefore be found in the electrode microstructure characteristics. It is of common knowledge, that particle and/or agglomerate size as well as porosity and layer thickness should be custom-tailored for both types of anodes, but numerical values of (I) volume fractions, (II) tortuosity, (III) surface areas and (IV) particle sizes have not been accessible so far.

There are basically two methods applicable to reconstruct the electrode microstructure of a porous electrode: focused ion beam (FIB) tomography and X-ray tomography [1–4]. Active material, carbon black and pore phase of a LiFePO₄-cathode, well-designed for high-power, was already reconstructed using FIB tomography. Microstructural features such as agglomerates differing in particle size and porosity, three-dimensional distribution of carbon fibers

Abbreviations: CT, computed tomography; EDT, Euclidean distance transform; EMC, ethyl methyl carbonate; FIB, focused ion beam; LiCoO₂, lithium cobalt oxide; LiFePO₄, lithium iron phosphate; SEM, scanning electron microscope.

* Corresponding author. Tel.: +49 721 6084 7599; fax: +49 721 608 4 74 92.

E-mail address: moses.ender@kit.edu (M. Ender).

for electron transport, and surface area accessible by electrolyte were reported in a previous work of our group [5]. But, as the average particle size of graphite anodes is approximately ten times larger, X-ray nano-tomography is the method of choice. Hence, volumes of $2.37 \cdot 10^6 \mu\text{m}^3$ and $1.27 \cdot 10^6 \mu\text{m}^3$ were analyzed in this work, large enough for being representative volume elements [6]. High resolutions of 273 nm and 233 nm voxel size were chosen, enabling an assessment of surface areas of graphite particles, accessible by the liquid electrolyte.

The investigated cells were state-of-the-art cylindrical cells with cell A denoting the high-power cell and cell B denoting the high-energy cell (Table 1).

2. Graphite negative electrodes and preparation

The high-power 18650 cell (cell A) in Table 1 was made of a LiFePO₄ cathode and a graphite anode, the high-energy 18500 cell (cell B) was made of LiCoO₂ and graphite. Both cell types were opened in an Argon filled glove box, the graphite anodes were rinsed with ethyl methyl carbonate (EMC) for removal of electrolyte and stored in a vacuum chamber to evaporate the EMC. The microstructure characteristics of both graphite anodes, denoted as anode A and anode B, were analyzed by scanning electron microscopy (SEM). SEM images of the surface, after removal of electrolyte and EMC, are shown in Fig. 1. There is no information available about the exact composition of the electrodes or about the properties of the used powders. As indicated by the characteristic shape of the open circuit potentials shown in Fig. 2, both anodes possess a graphitic structure. The minor differences in the shape of the different stages suggest a difference in the microscopic structure, e.g. crystallite size.

The SEM micrographs do not reveal specific features that are different between both anodes. Both consist of particles of irregular shape with sizes up to 20 μm, which are randomly arranged. In addition to the graphite particles, anode A shows some carbon fibers which are added to better connect the graphite particles. A difference in porosity, which might be expected, is not detectable. The similar appearing in SEM micrographs underlines the necessity of a three-dimensional reconstruction by tomography methods. As a next step, both anodes were prepared for X-ray tomography. For this purpose, the copper current collector had to be removed, as copper has a strong absorption coefficient at low X-ray energies. This was done by dipping the electrode into diluted hydrochloric acid (18%) for about 10 s, after which the coating was detached from the current collector. The porous graphite layer was then rinsed with distilled water and dried over night at 60 °C. After this treatment, the structural integrity of samples from anode A and anode B was ensured by SEM inspection. For anode A, both sides of the obtained porous graphite layer are shown in Fig. 3. The surface of anode A, which was directed towards the separator (Fig. 3a), has still the same appearance as in Fig. 1a. The opposite surface shown in Fig. 3b, formerly attached to the current collector, still shows the irregular binder network. This proves that the binder is not affected by exposing the electrode to diluted hydrochloric acid, thus the

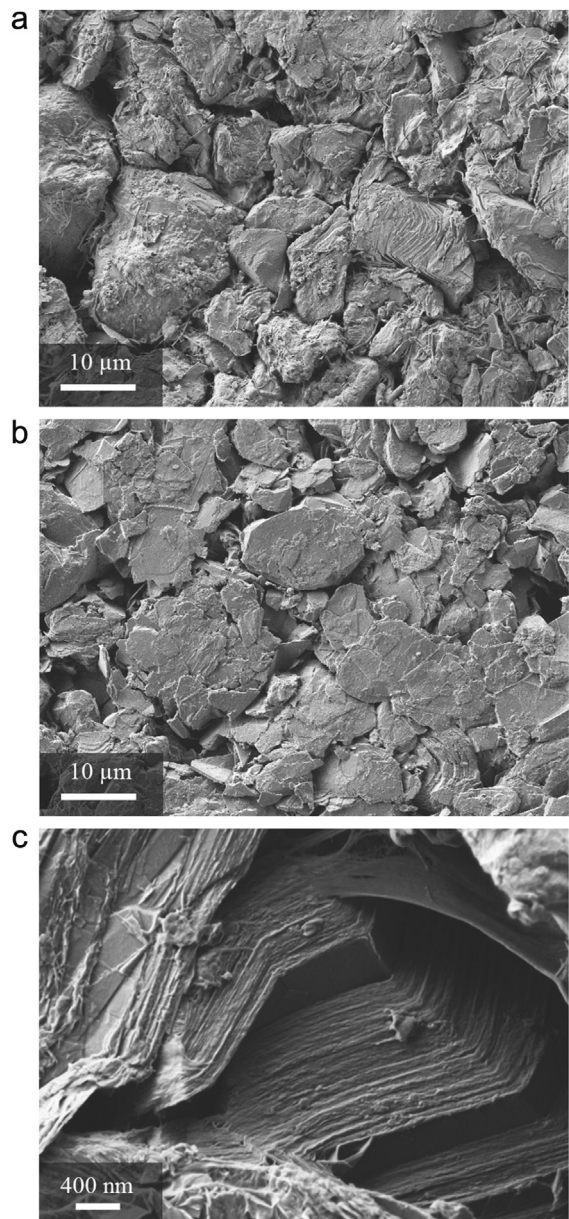


Fig. 1. SEM micrographs of the graphite anodes from (a) the high power cell (anode A from cell A) and (b) of the high energy cell (anode B from cell B). Additionally, a high-resolution image of the anode A is given (c), showing the slaty structure of a graphite particle edge.

binding forces between the individual graphite particles are still intact.

3. Reconstruction and segmentation

The porous graphite layers, which were detached from the current collector, were used for the actual X-ray computed tomography (CT). To mount the samples at the sample holder, they were further subdivided and suitable pieces were selected. The scan was done with a Bruker nano-CT SKYSCAN 2011 with a source voltage of 30 kV for anode A and 40 kV for anode B. Recording and reconstruction of the projection images was performed by our partner RJL Micro & Analytic GmbH (<http://www.rjl-microanalytic.de>). Cross-sections of the raw data from both anodes are shown in Fig. 4 and the properties of the reconstruction datasets are listed in

Table 1
Lithium-ion cells with high-power and high-energy characteristics.

	Cell A (high-power cell)	Cell B (high-energy cell)
Cell chemistry	LiFePO ₄ /graphite	LiCoO ₂ /graphite
Nominal capacity	1.1 Ah	1.5 Ah
Energy content	3.52 Wh	5.1 Wh
Mass	38.8 g	35 g
Maximum specific power	1800 W kg ⁻¹	290 W kg ⁻¹
Maximum specific energy	90.7 Wh kg ⁻¹	158 Wh kg ⁻¹
Anode thickness	47.7 μm	76.1 μm

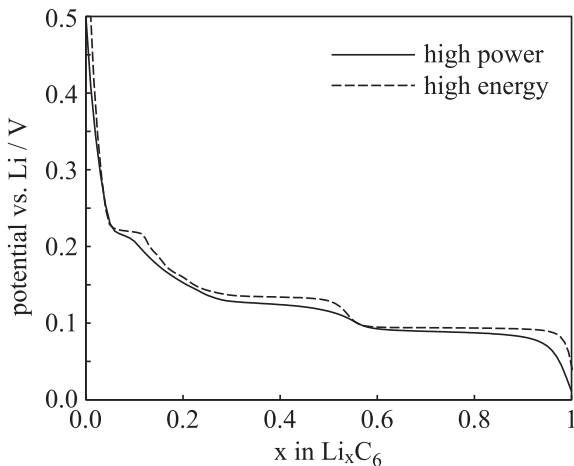


Fig. 2. Open circuit potentials of the graphite anodes obtained from half-cell measurements against a lithium metal electrode. Both anodes were discharged in approximately 100 steps with a potential relaxation step after each discharge step. Therefore, no overpotentials are included in the measurements.

Table 2. The volume sizes became extremely large, as almost the entire graphite anode layer thickness should be analyzed, being 43.7 μm for anode A and 72.2 μm for anode B. Furthermore, a base plane of 204 $\mu\text{m} \times$ 265 μm (anode A) and of 109 $\mu\text{m} \times$ 161 μm (anode B) was analyzed, large enough for determining statistically satisfying microstructure parameters. The resolution, with voxel

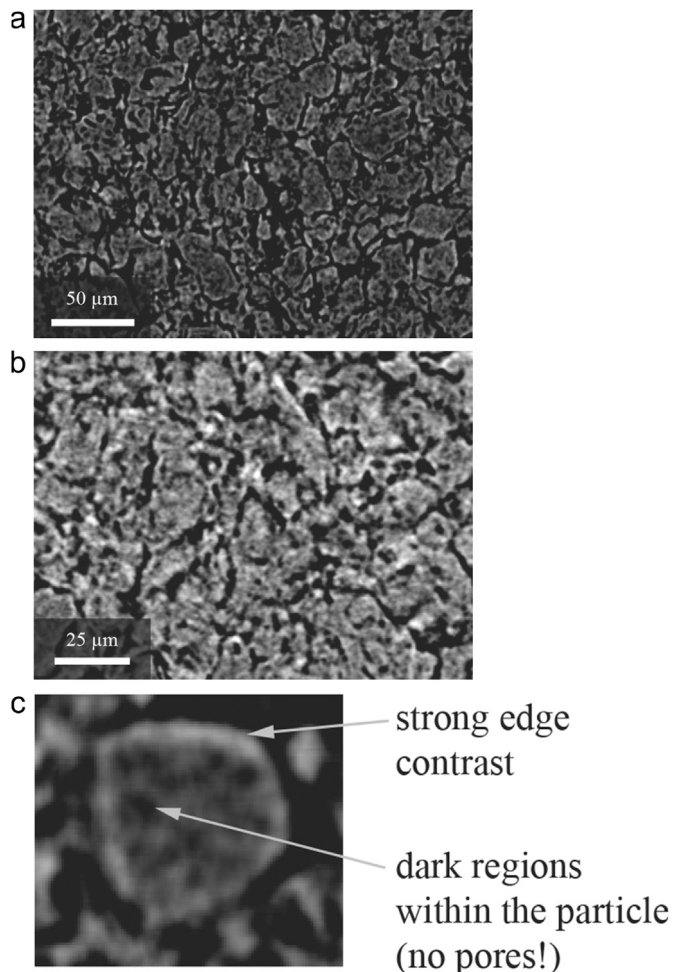


Fig. 4. Cross-section images of the X-ray tomography datasets of (a) anode A and (b) anode B. The graphite appears in gray and the porosity in black. A magnified particle (c) of anode A, showing the strong edge contrast of the particles and the darker regions within the particles which can erroneously be assigned as pores.

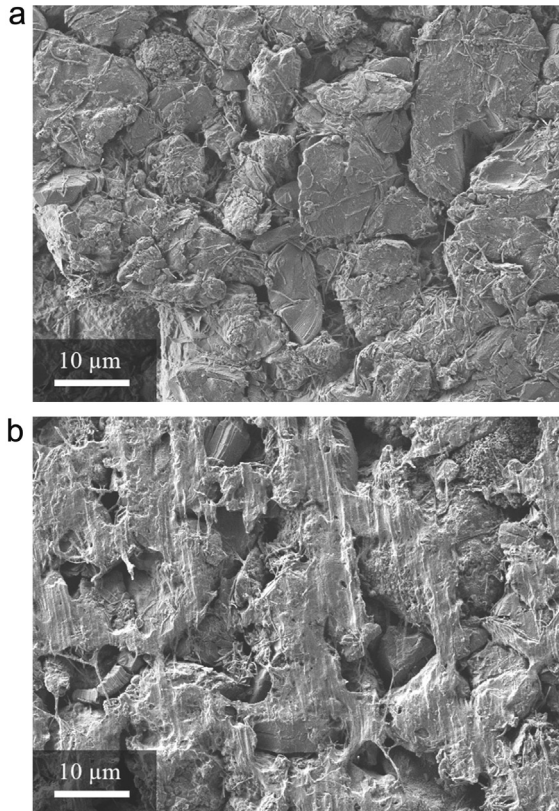


Fig. 3. SEM micrographs of the porous graphite structure of anode A, which was detached from the current collector. Neither the upper side (a) nor the lower side (b) show an influence of the hydrochloric acid on the structure. The lower side (b) shows remains from the binder which attached the coating to the copper current collector.

(volumetric pixel) sizes of 273 nm and 233 nm, is of particular importance for determining surface areas correctly.

The first step in data processing is the segmentation of the measured grayscale values by assigning each voxel to either graphite phase or pore phase. At the first glance, graphite and porosity in Fig. 4 are distinguishable quite well. However, the graphite particles appear darker towards the center than near the surface. This is a phase-contrast effect in addition to the absorption contrast [7], which is caused by the small X-ray source size and the high magnification. This enhanced edge contrast causes artifacts in the segmented image if a standard threshold segmentation is used. This is demonstrated in Fig. 5, where the peaks for graphite and pore phase are overlapping. In this histogram, the peak around the grayscale value of zero represents porosity, whereas the second peak is the graphite phase. Therefore, an alternative segmentation

Table 2
Comparison of the properties of the two anode reconstructions.

	Anode A	Anode B
Size (voxel)	$748 \times 971 \times 160$	$470 \times 692 \times 310$
Volume size	$204.2 \times 265.1 \times 43.7 \mu\text{m}^3$	$109.5 \times 161.2 \times 72.2 \mu\text{m}^3$
Resolution (voxel size)	273 nm	233 nm
X-ray energy	30 keV	40 keV

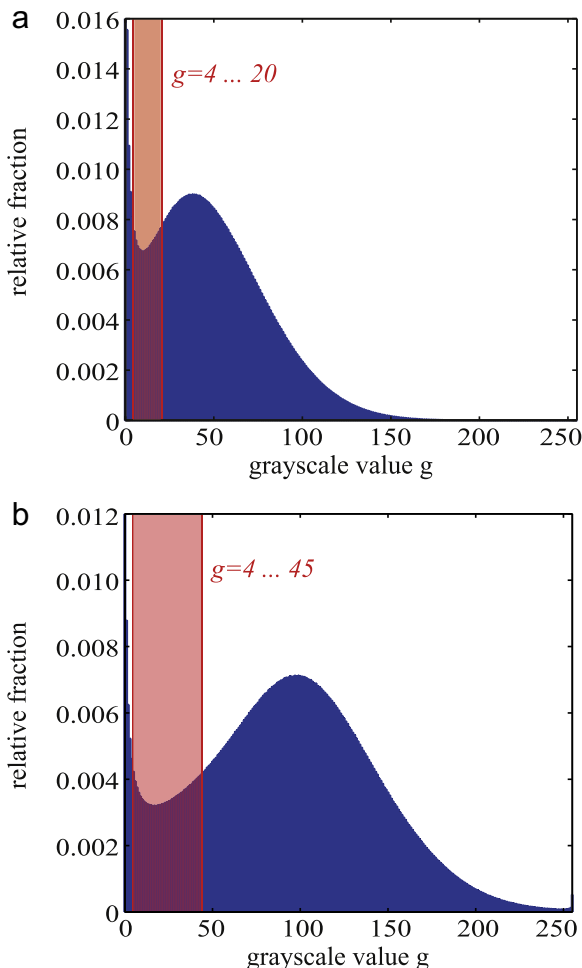


Fig. 5. Histograms of the three-dimensional datasets of (a) anode A and (b) anode B. The peak around the grayscale value of zero represents porosity, the second peak the graphite phase. The grayscale value range highlighted in red is not assigned in the initial segmentation but during the growth phase. (For interpretation of the references to color in this figure legend, the reader is referred to the web version of this article).

method becomes compulsory. We decided using a hysteresis segmentation, described for example in the book of Ohser and Schladitz [8], which was adapted for the graphite structures with a small modification.

In order to divide two material phases using a hysteresis approach, two threshold values g_1 and g_2 are required. The original hysteresis segmentation assigns everything above g_2 to the foreground [8]. In addition, adjacent regions with grayscale values between g_1 and g_2 are included in the foreground, which favors the foreground compared to the background. To overcome this, in this work, everything above g_2 is assigned to the material (in this case graphite) and everything below g_1 to porosity. In this initial segmentation, the grayscale values between g_1 and g_2 are not assigned yet (Fig. 5). In the next step, both regions expand iteratively and three-dimensionally into the regions not assigned yet, until either the next threshold value is reached or both material phases are in contact. If both phases are competing for a voxel, it is assigned to graphite if its grayscale value is larger than the mean value of g_1 and g_2 , otherwise it is assigned to porosity. This method successfully prevents the darker regions within the particles to be erroneously assigned as pores.

The results are binary three-dimensional datasets. As the noise present in the raw images can induce a noise in the segmented images, morphological operations are applied to the segmented

images. First, all isolated pores (pores within the graphite particles) were removed, as FIB polished cross-section images show no isolated porosity in the particles. Next, isolated graphite particles with a volume smaller than 1000 voxel were removed, as in a two-phase structure, every particle has to be in contact with at least one other particle. Fig. 6 shows cross-sections of the segmented anode datasets (same positions as Fig. 4), with the graphite in white and the porosity in black. The segmented datasets form the basis for analyzing the differences between the microstructures of the high-power and the high-energy cell anode.

4. Microstructure analysis

Understanding the microstructural design rules of the graphite-anode of a high-power cell (anode A) and of the high-energy cell

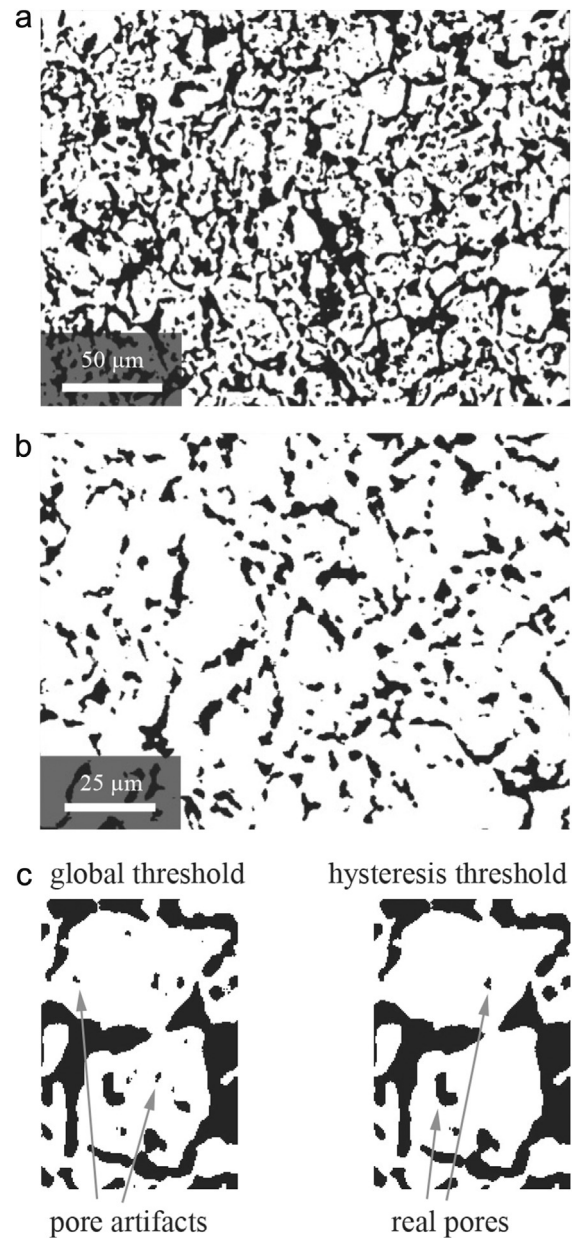


Fig. 6. Cross-section images through the structures of (a) anode A and (b) anode B after segmentation and morphological filtering. Additionally, a comparison (c) between the result of global threshold segmentation and hysteresis segmentation is given for a particle of anode A.

(anode B) requires a quantitative evaluation of the essential microstructure characteristics. For doing so, a number of microstructural parameter has to be calculated.

4.1. Volume fraction

The volume fractions ε_i of the material phases are calculated directly from the segmented three-dimensional dataset D_{jkl} . The entries of D_{jkl} equal 1 for graphite and 0 for porosity. Hence, the volume fractions can be calculated as:

$$\varepsilon_i = \frac{1}{N_x \cdot N_y \cdot N_z} \sum_{j,k,l} D_{j,k,l} \quad (1)$$

with N_x , N_y , N_z being the dimensions in x -, y - and z -direction respectively.

4.2. Tortuosity

The tortuosity τ of a porous structure can be interpreted in two ways. Either geometrically, where it is a measure for the elongation of a transport path due to the twisty structure of the pores, or in terms of an effective medium. In the latter case, it connects the intrinsic bulk conductivity σ_{bulk} (or diffusivity) with the effective conductivity σ_{eff} of the porous structure as an effective medium:

$$\sigma_{\text{eff},i} = \frac{\varepsilon_i}{\tau_i} \cdot \sigma_{\text{bulk},i} \quad (2)$$

Thereby, the subscript i denotes a specific material phase of a multi-phase structure and ε_i is its volume fraction. A good overview of the different tortuosity definitions is given by Ref. [9]. As in our previous work [2,5], equation (2) is used as the definition of tortuosity. For the calculation of the tortuosity, a simulation of the transport process is performed on the reconstructed microstructure, delivering the flux through the structure and with this the effective conductivity. Solving the transport equation

$$\nabla(-\sigma_{\text{bulk}} \nabla \phi) = 0 \quad (3)$$

was accomplished using a self-developed finite volume scheme implemented in MATLAB. Thereby, the voxel obtained from the reconstruction were used as cells for the calculation, which reflects the natural spatial resolution of the datasets. After assembling the system of equations, it was solved using the MINRES solver from MATLAB on a high-performance workstation [10,11]. For transport in z -direction (which is assumed to be perpendicular to the electrode), the boundary conditions were $\phi(z=0) = 0V$, $\phi(z=L_z) = 1V$ and $\vec{n} \cdot (\nabla \phi) = 0$ at all other boundaries, with \vec{n} being the normal vector of the specific boundary.

4.3. Surface area

The surface area is calculated using the marching cube algorithm [12]. This algorithm is very well suited for approximating a curved surface structure (Fig. 7a), as it calculates a triangulation of the surface. It is based on the idea that there are $2^8 = 256$ possibilities to distribute two materials at the corners of a cube. By exploiting the cubic symmetry, these 256 cases can be reduced to 15 fundamental cases with well-defined cutting planes through the cubes (Fig. 7b). The surface areas of the basic cutting planes have to be calculated only once. The surface area of the whole structure is calculated by going over all possible cubes of eight neighboring voxel in the structure while adding the surface areas of the corresponding basic cases.

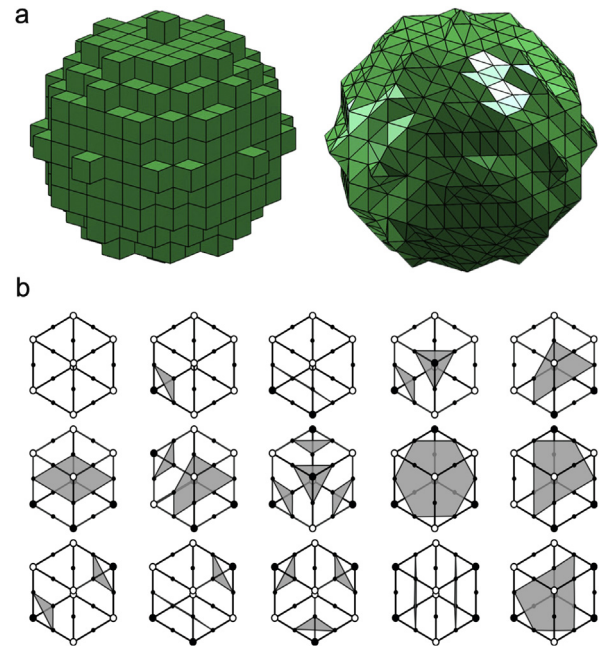


Fig. 7. While the voxel representation (a) of a structure leads to an overestimation of the surface area, a much better approximation of the smooth surface is obtained by using a triangulation of the surface based on the marching cube algorithm. The 15 different possibilities of cutting a cube consisting of eight voxel are shown in (b) with the planes separating material from porosity shown in gray.

In order to get a property which can be compared between different microstructures, it is useful to calculate the volume specific surface area $\mathcal{A}_{\text{spec}}$ which is the internal surface area within a volume:

$$\mathcal{A}_{\text{spec}} = \frac{A_{\text{internal}}}{V} \quad (4)$$

Here, A_{internal} is the absolute internal surface area of the investigated volume V without the outer boundaries. This method was used previously by our group to calculate surface areas of cathodes for solid oxide fuel cells [13] and of the LiFePO₄ cathode for the same high-power 18650 cell investigated in this work [5].

4.4. Particle size

The particle size is calculated on basis of the Euclidean distance transform (EDT). We already applied this method for the LiFePO₄ cathode of the high-power 18650 cell [5].

When the EDT is applied to a binary three-dimensional image (Fig. 8a), for each voxel with value 1 the Euclidean distance to the closest voxel with value 0 is calculated. The result of this transform is a three-dimensional distance map (Fig. 8b) where the value of each voxel corresponds to the distance to the closest voxel outside the particle. Hence, the value at a maximum in the distance map corresponds to the radius of the largest sphere than can be placed inside the particle. For a robust calculation of the particle size, it is necessary to detect multiple maxima within a particle (Fig. 8c) and to merge them. This is done by discarding all but the maximum with the largest value, if their distances are smaller than a given value.

The sizes of the spheres defined by the remaining maxima (Fig. 8d) are taken as measure of the particle sizes. The bias between the calculated and the actual particle sizes are corrected by a linear correction function [5]. Based on the individual particle sizes,

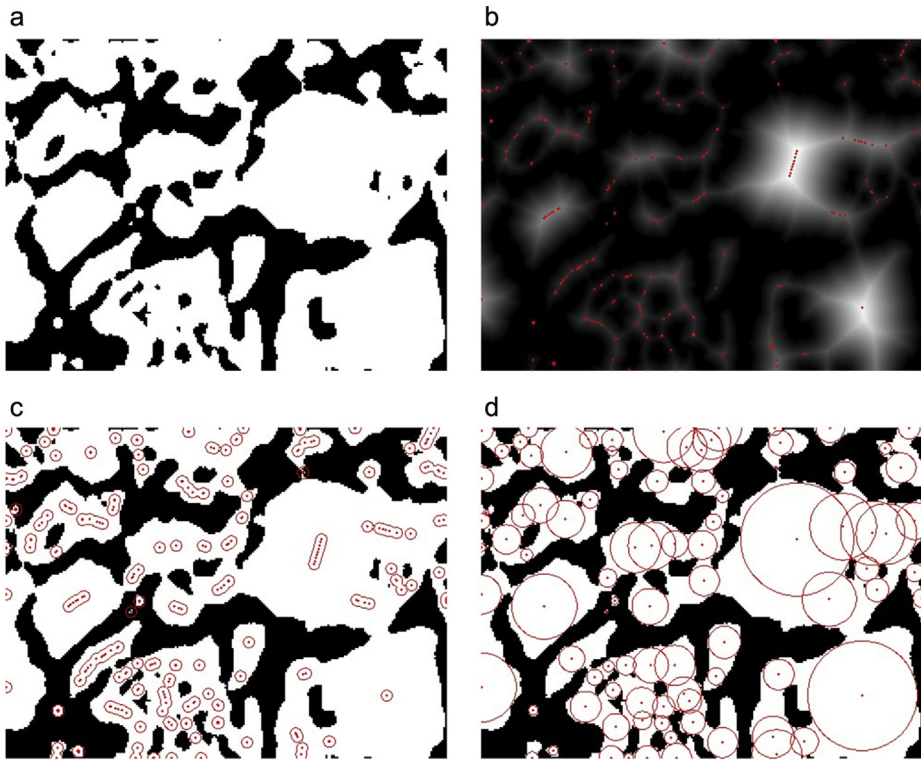


Fig. 8. Two-dimensional illustration of the particle size calculation of a binary image (a) based on the Euclidean distance transform. Neighboring maxima in the distance map (b) are merged if their distance is smaller than a given value (c). The results are the largest spheres that can be placed within the particles (d).

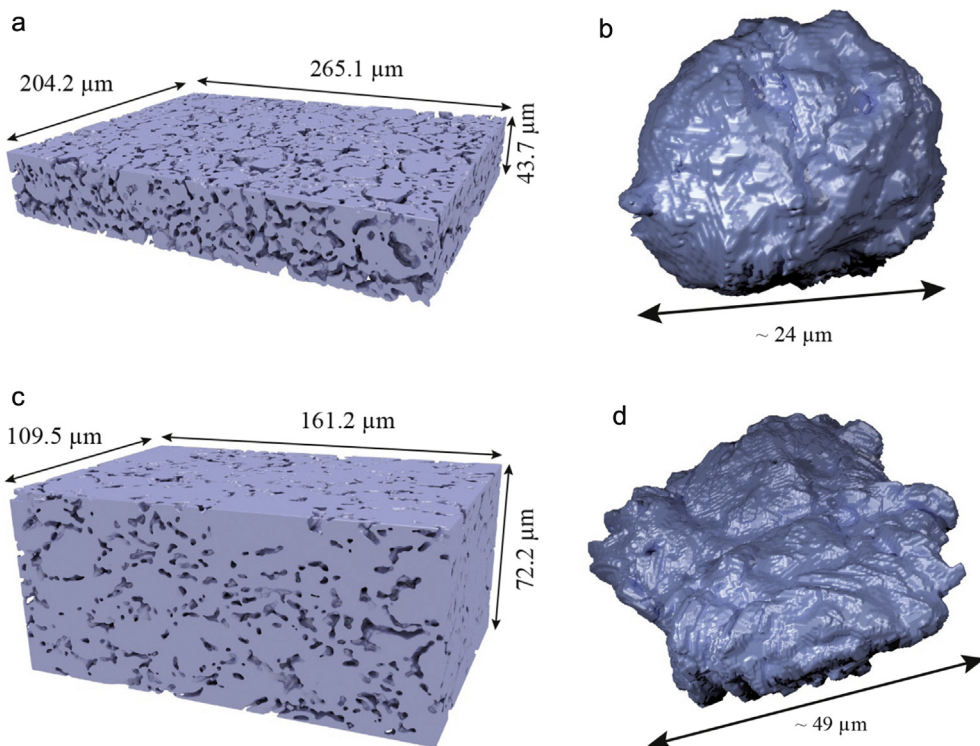


Fig. 9. Three-dimensional rendering of the reconstructed volumes of (a) the high-power anode (anode A) and (c) the high-energy anode (anode B). The graphite is shown in a bluish gray color while the porosity appears transparent. Additionally, single particles extracted from anode A (b) and anode B (d) give details on particle shape and surface characteristics. Thus, resolution given by a voxel size of 273 nm and 233 nm becomes visible. (For interpretation of the references to color in this figure legend, the reader is referred to the web version of this article).

the average particle size and the particle size distribution are then calculated.

5. Results and discussion

The methods described above can now be used to characterize the microstructures of the high-power anode (cell A) and of the high-energy anode (cell B). A three-dimensional visualization of both reconstructed volumes is given in Fig. 9. The microstructure parameters (I) volume fractions, (II) tortuosity, (III) surface areas and (IV) particle sizes are listed in Table 3.

Volume fractions and porosity

As already indicated by the two cross-section images in Fig. 6, the reconstruction confirms a pronounced difference in volume fractions of active material and pore phase and thus in porosity between anode A and B. The high-energy anode B reveals a porosity of 18.2%. This can be understood in terms of the higher graphite volume fraction that is necessary to achieve a sufficiently high anode capacity. It is consistent with the result found by Shearing et al. who determined the porosity of another type of high-energy anode to be 15.4% [3]. On the contrary, the porosity of 35.2% for the high-power anode A is almost twice as high, thus providing more space for the liquid electrolyte inside the porous anode structure. This allows for higher C-rates without depletion of the salt concentration in the electrolyte.

Tortuosity of pore phase

The tortuosity of the pore phase is strongly correlated to porosity itself, as a lower porosity naturally implies a higher tortuosity. This leads to tortuosity values of 11.28 for anode B and 2.72 for anode A. Both tortuosity values exceed by far the value of 1.6 reported by Shearing et al. [3]. This can be explained by the fact, that Shearing applied a geometrical definition for calculating the tortuosity, which completely disregards existing transport constrictions in the pore space. Using our approach for calculating tortuosity, one can interpret the pronounced difference between anode A and B in terms of effective transport parameters (ε/τ , see equation (2)). Interesting enough, this ratio ε/τ is 7.9 times larger within the electrolyte-filled pores of the high-power anode A than in the high-energy anode B. Furthermore, the entire thickness of the graphite layer is 47.7 μm for anode A, but 76.1 μm for anode B. Both, layer thickness and ε/τ indicate that electrolyte transport loss is much higher in anode B.

Volume specific graphite surface and total surface area

At first, it surprises that the volume specific surface areas $\mathcal{A}_{\text{spec}} = 0.40 \mu\text{m}^{-1}$ for the high-power anode A and

$\mathcal{A}_{\text{spec}} = 0.36 \mu\text{m}^{-1}$ for the high-energy anode B differ only by 10%, even though their graphite volume fractions differ by nearly 30%. Furthermore, because of the rather thick anode B it adds up to a total surface area (per cm^2 electrode) of 27.32 cm^2 , which is 45% more than for anode A. However, as the high-rate capability of cell B is inferior to cell A, this clearly highlights that surface area is not the only performance determining factor of a graphite electrode.

Average particle size and volume weighted particle size

Average particle size is similar for anode A (4.24 μm) and for anode B (4.32 μm). These values are comparable with the particle size (4.78 μm) determined by Shearing et al. for a high-energy graphite anode [3]. However, if the particle sizes obtained by a volume weighted averaging are compared, these values become distinctively larger for anode B (9.12 μm) than for anode A (6.75 μm). This indicates that the electrode structure of anode B must contain also large particles that might be small in number but represent a relatively large volume fraction. The particle size distribution shown in Fig. 10 confirms this assumption: it is wider for anode B and extends to 25 μm . This allows for a higher packing density and hence for a high graphite volume fraction and a low porosity. The well-packed arrangement of the graphite particles does also influence the average pore size, which is smaller in anode B (1.98 μm) than in anode A (2.95 μm). However, as already discussed above, this is at the cost of a high tortuosity of pore phase of 11.18 compared to 2.72.

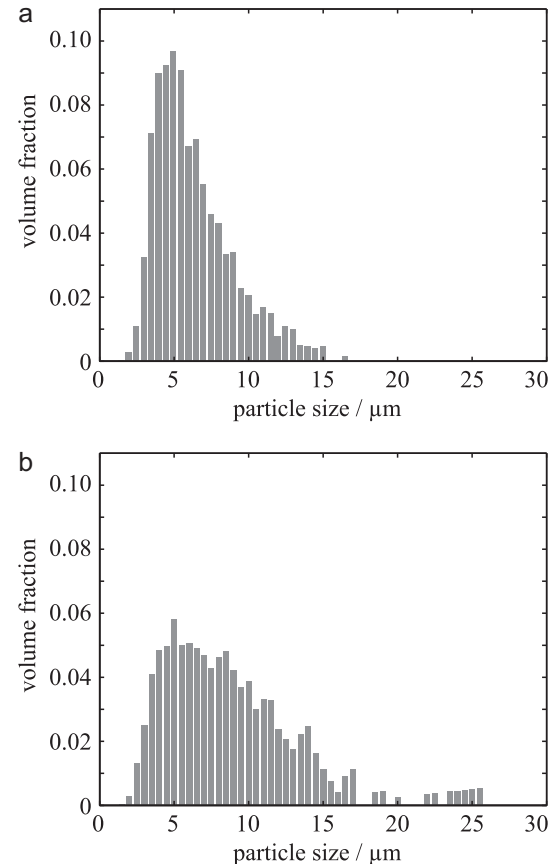


Fig. 10. Particle size distributions of the graphite of (a) the high-power anode A and (b) the high-energy anode B. The average particle sizes for anode A (4.24 μm) and anode B (4.32 μm) are similar, however, particle size distribution is wider for anode B and extends to 25 μm . This allows for a higher packing density and hence for a high graphite volume fraction and a low porosity.

Table 3

Microstructure parameter sets of the two graphite anodes originating from cylindrical cells, anode A: high-power, anode B: high-energy.

	Anode A (high-power)	Anode B (high-energy)
Graphite volume fraction	0.648	0.818
Porosity	0.352	0.182
Tortuosity of pore phase	2.72	11.18
$\sigma_{\text{eff}}/\sigma_0 = \varepsilon/\tau$	0.129	0.016
Volume specific graphite surface	$0.40 \mu\text{m}^{-1}$	$0.36 \mu\text{m}^{-1}$
Total surface area (per cm^2 electrode)	18.84 cm^2	27.32 cm^2
Average particle size	4.24 μm	4.32 μm
Volume weighted particle size	6.75 μm	9.12 μm
Average pore size	2.95 μm	1.98 μm

6. Conclusion

Graphite negative electrodes of high-power and high-energy lithium-ion cylindrical cells have been three-dimensionally reconstructed by X-ray nano-tomography using a commercial lab-scale device. This method was proven to be more suitable than focused ion beam (FIB) tomography, as average particle sizes of graphite anodes are approximately ten times larger than that of intercalation compounds for cathodes. Hence, quite big volumes of $2.37 \cdot 10^6 \mu\text{m}^3$ and $1.27 \cdot 10^6 \mu\text{m}^3$ had to be analyzed to cover the entire thickness of both anode layers. High resolutions of 273 nm and 233 nm voxel size were chosen for assessing volume specific graphite surface area, among other parameters, precisely. A hysteresis segmentation method was adapted for segmentation, featuring a symmetrical growing of both graphite and pore phase. Surface areas were calculated using the marching cube algorithm, particle sizes were calculated based on the Euclidean distance transform (EDT) and tortuosity values were calculated by solving the transport equation using a finite volume scheme in MATLAB.

In this work, extensive data sets from a high-power and a high-energy cell were directly compared for the first time, illustrating the different design aspects of both anode types, regarding:

- Active material volume fraction of the high-energy graphite anode is 17% vol. higher and porosity is 17% vol. lower, compared to the high-power graphite anode.
- Tortuosity of the pore phase of the high-energy graphite anode is 311% larger, compared to the high-power graphite anode.
- Volume specific surface area of the high-energy graphite anode is 10% lower compared to the high-power graphite anode, whereas
- Overall surface area of the high-energy graphite anode is 45% higher compared to the high-power graphite anode.
- Average particle sizes are similar, but a volume-averaged mean particle size of 9.12 μm for the high-energy graphite anode instead of 6.75 μm for the high-power graphite anode indicates a different packing design. This is backed up by the particle size distributions, which differ significantly in number and size of the largest particles.

The analysis of these microstructure parameters leads to the assumption, that the electrolyte transport is limited by the pore structure of the high-energy graphite anode, as the effective transport parameters are giving evidence for it. The microstructure parameters (I) volume fractions, (II) tortuosity, (III) surface areas and (IV) particle sizes provide now a profound basis for further research, i.e., electrochemical performance analysis using impedance spectroscopy and modeling, using homogenized porous electrode models.

Acknowledgements

The authors thank Dr. Markus Heneka from RJL Micro & Analytic GmbH for discussions and assistance with the anode reconstructions.

References

- [1] J.R. Wilson, J.S. Cronin, S.A. Barnett, S.J. Harris, *J. Power Sources* 196 (2011) 3443.
- [2] M. Ender, J. Joos, T. Carraro, E. Ivers-Tiffée, *Electrochim. Commun.* 13 (2011) 166.
- [3] P.R. Shearing, L.E. Howard, P.S. Jorgensen, N.P. Brandon, S.J. Harris, *Electrochim. Commun.* 12 (2010) 374.
- [4] B. Yan, C. Lim, L. Yin, L. Zhu, *J. Electrochem. Soc.* 159 (2012) A1604–A1614.
- [5] M. Ender, J. Joos, T. Carraro, E. Ivers-Tiffée, *J. Electrochim. Soc.* 159 (2012) A972–A980.
- [6] J. Joos, M. Ender, T. Carraro, A. Weber, E. Ivers-Tiffée, *Electrochim. Acta* 82 (2012) 268.
- [7] S. Mayo, T. Davis, T. Gureyev, P. Miller, D. Paganin, A. Pogany, A. Stevenson, S. Wilkins, *Opt. Express* 11 (2003) 2289.
- [8] J. Ohser, K. Schladitz, *3D Images Of Materials Structures: Processing And Analysis*, John Wiley & Sons, Weinheim, 2009.
- [9] L. Shen, Z. Chen, *Chem. Eng. Sci.* 62 (2007) 3748.
- [10] C.C. Paige, M.A. Saunders, *SIAM J. Numer. Analysis* 12 (1975) 617.
- [11] R. Barrett, M.W. Berry, T.F. Chan, J. Demmel, J. Donato, J. Dongarra, V. Eijkhout, R. Pozo, C. Romine, H. Van der Vorst, *Templates For The Solution Of Linear Systems: Building Blocks For Iterative Methods*, Society for Industrial and Applied Mathematics, Philadelphia, 1994.
- [12] W.E. Lorensen, H.E. Cline, *Comput. Graph.* 21 (1987) 163.
- [13] J. Joos, T. Carraro, M. Ender, B. Rüger, A. Weber, E. Ivers-Tiffée, *ECS Trans.* 35 (2011) 2357.